Self-interference fluorescence microscopy: three dimensional fluorescence imaging without depth scanning

Self-interference fluorescence microscopy: three dimensional fluorescence imaging without depth scanning

Mattijs de Groot,[1,*] Conor L. Evans,[2] and Johannes F. de Boer[1]

[1]*Institute for Lasers, Life and Biophotonics Amsterdam, Department of Physics and Astronomy, VU University Amsterdam, de Boelelaan 1081, 1081 HV Amsterdam, The Netherlands*

[2]*Wellman Center for Photomedicine, Harvard Medical School, Massachusetts General Hospital, 40 Blossom St, BAR410, Boston, Massachusetts 02114, USA*

[*]*m.de.groot@vu.nl*

Abstract: We present a new method for high-resolution, three-dimensional fluorescence imaging. In contrast to beam-scanning confocal microscopy, where the laser focus must be scanned both laterally and axially to collect a volume, we obtain depth information without the necessity of depth scanning. In this method, the emitted fluorescence is collected in the backward direction and is sent through a phase plate that encodes the depth information into the phase of a spectrally resolved interference pattern. We demonstrate that decoding this phase information allows for depth localization accuracy better than 4 µm over a 500 µm depth-of-field. In a high numerical aperture configuration with a much smaller depth of field, a localization accuracy of tens of nanometers can be achieved. This approach is ideally suited for miniature endoscopes, where space limitations at the endoscope tip render depth scanning difficult. We illustrate the potential for 3D visualization of complex biological samples by constructing a three-dimensional volume of the microvasculature of *ex vivo* murine heart tissue from a single 2D scan.

OCIS codes: (110.3175) Interferometric imaging;(170.6900) Three-dimensional microscopy; (170.2520) Fluorescence microscopy; (170.1790) Confocal microscopy.

References and links

1. L. Sampath, S. Kwon, S. Ke, W. Wang, R. Schiff, M. E. Mawad, and E. M. Sevick-Muraca, "Dual-labeled trastuzumab-based imaging agent for the detection of human epidermal growth factor receptor 2 overexpression in breast cancer," J. Nucl. Med. **48**(9), 1501–1510 (2007).
2. P. Zou, S. Xu, S. P. Povoski, A. Wang, M. A. Johnson, E. W. Martin, V. Subramaniam, R. Xu, and D. Sun, "Near-infrared fluorescence labeled anti-TAG-72 monoclonal antibodies for tumor imaging in colorectal cancer xenograft mice," Mol. Pharm. **6**, 428–440 (2009).
3. E. A. te Velde, T. Veerman, V. Subramaniam, and T. Ruers, "The use of fluorescent dyes and probes in surgical oncology," Eur. J. Surg. Oncol. **36**(1), 6–15 (2010).
4. A. G. T. Terwisscha van Scheltinga, G. M. van Dam, W. B. Nagengast, V. Ntziachristos, H. Hollema, J. L. Herek, C. P. Schröder, J. G. W. Kosterink, M. N. Lub-de Hoog, and E. G. E. de Vries, "Intraoperative near-infrared fluorescence tumor imaging with vascular endothelial growth factor and human epidermal growth factor receptor 2 targeting antibodies," J. Nucl. Med. **52**(11), 1778–1785 (2011).
5. G. M. van Dam, G. Themelis, L. M. Crane, N. J. Harlaar, R. G. Pleijhuis, W. Kelder, A. Sarantopoulos, J. S. de Jong, H. J. Arts, A. G. van der Zee, J. Bart, P. S. Low, and V. Ntziachristos, "Intraoperative tumor-specific fluorescence imaging in ovarian cancer by folate receptor-α targeting: first in-human results," Nat. Med. **17**(10), 1315–1319 (2011).
6. K. E. Drabe, G. Cnossen, and D. A. Wiersma, "Localization of spontaneous emission in front of a mirror," Opt. Commun. **73**(2), 91–95 (1989).
7. A. K. Swan, L. A. Moiseev, C. R. Cantor, B. Davis, S. B. Ippolito, W. C. Karl, B. B. Goldberg, and M. S. Unlu, "Toward nanometer-scale resolution in fluorescence microscopy using spectral self-interference," IEEE J. Sel. Top. Quantum Electron. **9**(2), 294–300 (2003).

#166541 - $15.00 USD Received 12 Apr 2012; revised 23 May 2012; accepted 25 May 2012; published 22 Jun 2012

8. M. Dogan, M. I. Aksun, A. K. Swan, B. B. Goldberg, and M. S. Unlü, "Closed-form representations of field components of fluorescent emitters in layered media," J. Opt. Soc. Am. A **26**(6), 1458–1466 (2009).
9. A. Bilenca, A. Ozcan, B. Bouma, and G. Tearney, "Fluorescence coherence tomography," Opt. Express **14**(16), 7134–7143 (2006).
10. G. Shtengel, J. A. Galbraith, C. G. Galbraith, J. Lippincott-Schwartz, J. M. Gillette, S. Manley, R. Sougrat, C. M. Waterman, P. Kanchanawong, M. W. Davidson, R. D. Fetter, and H. F. Hess, "Interferometric fluorescent super-resolution microscopy resolves 3D cellular ultrastructure," Proc. Natl. Acad. Sci. U.S.A. **106**(9), 3125–3130 (2009).
11. B. Park, M. C. Pierce, B. Cense, S.-H. Yun, M. Mujat, G. Tearney, B. Bouma, and J. de Boer, "Real-time fiber-based multi-functional spectral-domain optical coherence tomography at 1.3 microm," Opt. Express **13**(11), 3931–3944 (2005).
12. S. L. K. Bowers, T. K. Borg, and T. A. Baudino, "The dynamics of fibroblast-myocyte-capillary interactions in the heart," Ann. N. Y. Acad. Sci. **1188**(1), 143–152 (2010).
13. I. J. LeGrice, B. H. Smaill, L. Z. Chai, S. G. Edgar, J. B. Gavin, and P. J. Hunter, "Laminar structure of the heart: ventricular myocyte arrangement and connective tissue architecture in the dog," Am. J. Physiol. **269**(2 Pt 2), H571–H582 (1995).

1. Introduction

Fluorescence microscopy has revolutionized biology and biomedicine during the past decades through the ability to specifically label and image cell structures or proteins of interest. With the development of clinically approved near-infrared fluorescent probes conjugated to therapeutic or diagnostic agents, a similar development is expected in the coming years in clinical medicine [1–5]. To bring these translational advances in fluorescence labeling to clinical practice, however, requires a new class of miniature endoscopic imaging systems that will enable clinicians to rapidly visualize the three-dimensional distribution of fluorescence labels *in situ*.

Self-interference fluorescence microscopy (SIFM) extends the capabilities of confocal microscopy by providing depth sensitivity much better than the axial spot size. Fluorescence self-interference has been explored before [6–10], but these approaches were based on a transmission configuration and therefore could not easily be incorporated into conventional or miniature imaging systems. Our SIFM method addresses this challenge by collecting the fluorescence in the backward direction and phase-encoding the depth information through the use of a phase plate (e.g., a glass plate with an opening) placed into the beam path. This plate presents the photons emitted by a fluorophore with two alternative paths that then interfere upon coupling into a single mode fiber that acts as a pinhole. The path length difference between the two paths gives rise to depth-dependent interference as a function of wavelength, where moving the fluorescent source axially through the beam waist causes the wavelength-dependent interference pattern to undergo a phase shift. The lateral resolution in SIFM is determined by both the beam waist and the fiber core aperture size, similar to confocal microscopy.

2. Theory

2.1 Principle of SIFM

Figure 1 illustrates the principle of self-interference fluorescence microscopy. The SIFM spectrum as a function of wave number k is given by:

$$I_{\text{sifm}}(k) = C \cdot I_{\text{source}}(k)\left(1 - \tfrac{A}{2} + \tfrac{A}{2}\cos\left(k\left(d + \Delta_{\text{opl}}(\delta)\right)\right)\right) \quad (1)$$

where $I_{\text{SIFM}}(k)$ is the intensity detected at wave number k, C is the total collection efficiency of the confocal imaging system, and $I_{\text{source}}(k)$ is the intensity emitted by the source at wave number k. A is the modulation depth of the self-interference, which varies between 0 and 1. It is based on the ratio of the field amplitudes integrated over the inner and outer sections of the phase plate. d is the optical thickness of the phase plate. Finally, $\Delta_{\text{opl}}(\delta)$ is the average *extra*

#166541 - $15.00 USD Received 12 Apr 2012; revised 23 May 2012; accepted 25 May 2012; published 22 Jun 2012

path length difference (on the order of a fraction of the wavelength) that is induced by the wavefront curvature between the photons passing through the inner and outer sections of the phase plate (see Fig. 1). $\Delta_{opl}(\delta)$ is a function of the defocus distance δ, the distance between the source and the focal plane of the objective. A negative value for δ indicates that the source is further away from the objective than the focal plane, whereas a positive value indicates that that the source is closer to the objective. When the phase plate radius is optimal ($A = 1$), on average only half of the photons get accepted by the core of the single mode fiber because of constructive and destructive interference (the other half couples into the cladding). The cosine term in Eq. (1) describes the modulation, indicating that depth information is carried by half of the collected photons. In the shot noise limit the signal to noise ratio (SNR) of the interferometric signal is therefore given by $\frac{1}{2}N/\sqrt{N} = \frac{1}{2}\sqrt{N}$, where N is the total number of collected photons. Experimentally, the SNR is determined by the ratio of the length of the complex Fourier component at the modulation frequency $kd/2\pi$ and the background level in the vicinity of the modulation frequency. The phase is determined by the arctangent of the imaginary over the real part of the Fourier component at the modulation frequency. This phase encodes a single depth position. In the presence of multiple fluorescent sources at different depths, the intensity weighted mean depth position is calculated instead. The minimum detectable phase difference and therefore the depth sensitivity of SIFM is fundamentally limited by the phase noise σ_ϕ, which is a function of the signal to noise ratio via

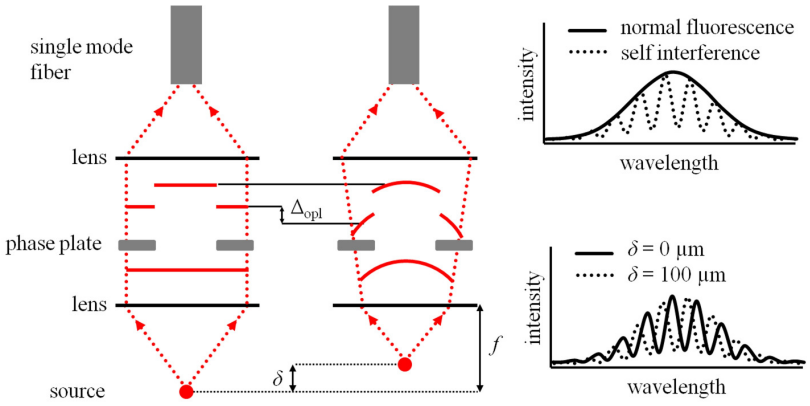

Fig. 1. Principle of SIFM. Light from a fluorescent source in the sample is collimated by the objective lens and passes through a phase plate. The phase plate consists of an inner and an outer ring of different optical thickness, introducing two alternative optical paths. The wave front before and after the phase plate is drawn as a solid red line. The light passing through the thicker outer ring of the phase plate is retarded with respect to the light passing through the hole in the center. The light is focused on a single mode optical fiber, acting as a pinhole. The interference due to the optical path difference leads to a modulation on the detected fluorescence spectrum: for certain wavelengths the interference is destructive while for others it is constructive (top graph). The period of the spectral modulation is determined by the thickness of the plate. The modulation depth depends on the ratio of the integrated amplitude of the source field over the central disk of the phase plate and the outer ring, respectively. When the source is exactly in focus (δ = 0 µm) the wavefronts are flat. When the source is out of focus (δ = 100 µm) the wavefronts are curved (shown exaggerated). This leads to a small extra path length difference $\Delta_{opl}(\delta)$ and to a shift in the phase of the self-interference spectrum (bottom graph). The phase therefore directly encodes the axial position of the fluorescent source.

#166541 - $15.00 USD Received 12 Apr 2012; revised 23 May 2012; accepted 25 May 2012; published 22 Jun 2012

$\sigma_\phi = 2^{-1/2} \cdot SNR^{-1}$ [11]. SIFM will detect the intensity weighted average depth location when multiple fluorescent sources are present at different depths within the depth-of-field. The technique therefore works best for relatively sparse samples.

2.2 Ray optics model

We describe the phase response of the self-interference spectrum as a function of defocus with the following numerical model. This simple model gives an intuitive, geometrical description for the phase shift as a function of depth and agrees very well with the experimental data up to a defocus of twice the Rayleigh length Z_R.

Figure 2 displays the optical layout that is the basis for the ray optics calculations of the phase of the self interference as a function of defocus d. The source of the fluorescence is located a distance δ from the focal plane of the objective $\mathbf{L_0}$ with a focal length f_0. A telescope consisting of two lenses $\mathbf{L_1}$ and $\mathbf{L_2}$ with focal lengths f_1 and f_2 respectively magnifies the beam by a factor $m = -f_2/f_1$. The telescope images the back focal plane of the objective onto the phase plate PP. The phase plate consists of an inner disk (or hole) with a diameter $2r$ and an outer ring (annulus) that has a different optical thickness. For the purpose of this model we neglect the refraction in the phase plate and consider it as an element that adds a fixed optical delay to all rays passing through the outer ring.

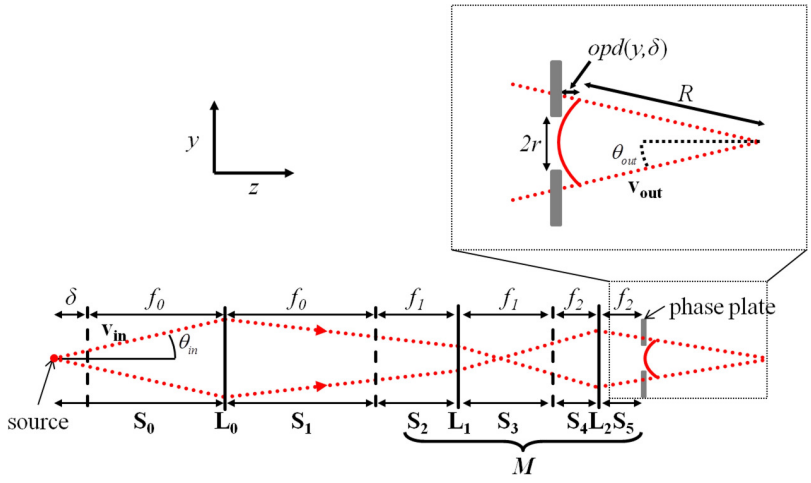

Fig. 2. Schematic representation of the ray matrix model. The rays $\mathbf{v_{in}}$ emitted by a source at a defocus distance δ from the focal plane of the objective $\mathbf{L_0}$ are traced by multiplication with the free space propagation matrices $\mathbf{S_i}$ and the lens matrices $\mathbf{L_i}$. From the position $\mathbf{v_{out}}$ and the angle θ_{out} we can calculate the radius of curvature R of the wave front at the phase plate. This allows us to calculate the optical path delay $opd(y,\delta)$ which we define as the difference in optical path to the phase plate between a ray intersecting the phase plate at y and the chief ray for which $y = 0$. Averaging of $opd(y,\delta)$ over the inner and outer sections of the phase plate now yields $\Delta_{opl}(\delta)$ the *extra* path length difference between the field passing through the center and the field passing through the edge of the plate that is caused by the wave front curvature (see Fig. 1).

The propagation of a ray through this optical system from the source to the phase plate can be described by the following ray transfer matrices:

$$\mathbf{S}_i = \begin{pmatrix} 1 & d_i \\ 0 & 1 \end{pmatrix}, \mathbf{L}_i = \begin{pmatrix} 1 & 0 \\ -\frac{1}{f_i} & 1 \end{pmatrix} \quad (2)$$

and the ray vector

#166541 - $15.00 USD Received 12 Apr 2012; revised 23 May 2012; accepted 25 May 2012; published 22 Jun 2012

$$\mathbf{v}_i = \begin{pmatrix} y_i \\ \theta_i \end{pmatrix}. \tag{3}$$

Here $\mathbf{S}_i$ is the i'th free space propagation matrix with d_i the propagation distance. $\mathbf{L}_i$ is the thin lens matrix with f_i the focal length. $\mathbf{v}_i$ is a ray with y_i the position and θ_i the angle of the ray. We set $d_0 = f_0 - \delta$, $d_1 = f_0$, $d_2 = d_3 = f_1$, $d_4 = d_5 = f_2$, (i.e. all optical elements are telecentrically aligned and δ describes the distance of the source from the focal plane of the objective). We need to find the average optical path difference introduced by the defocus δ between the sections of the beam that pass through the inner and outer rings of the phase plate respectively. The full ray propagation is described by the following equation:

$$\mathbf{v}_{out} = \mathbf{S}_5\mathbf{L}_2\mathbf{S}_4\mathbf{S}_3\mathbf{L}_1\mathbf{S}_2\mathbf{S}_1\mathbf{L}_0\mathbf{S}_0\mathbf{v}_{in} = \begin{pmatrix} 0 & -\frac{f_0 f_2}{f_1} \\ \frac{f_1}{f_0 f_2} & \frac{f_1 \delta}{f_0 f_2} \end{pmatrix} \mathbf{v}_{in}. \tag{4}$$

The telescope $\mathbf{S}_5\mathbf{L}_2\mathbf{S}_4\mathbf{S}_3\mathbf{L}_1\mathbf{S}_2$ can be described as a magnification

$$\mathbf{M} = \begin{pmatrix} m & 0 \\ 0 & \frac{1}{m} \end{pmatrix} \tag{5}$$

where $m = -\frac{f_2}{f_1}$, simplifying Eq. (4) to

$$\mathbf{v}_{out} = \mathbf{M}\mathbf{S}_1\mathbf{L}_0\mathbf{S}_0\mathbf{v}_{in} = \begin{pmatrix} 0 & mf_0 \\ -\frac{1}{mf_0} & -\frac{\delta}{mf_0} \end{pmatrix} \mathbf{v}_{in} = \begin{pmatrix} mf_0\theta_{in} \\ -\frac{y_{in} + \delta\theta_{in}}{mf_0} \end{pmatrix}. \tag{6}$$

When $\mathbf{v}_{in} = \begin{pmatrix} 0 \\ \theta_{in} \end{pmatrix}$, i.e. when a ray comes from the lateral focus, $\mathbf{v}_{out}$ becomes

$$\mathbf{v}_{out} = \begin{pmatrix} mf_0\theta_{in} \\ -\frac{\delta\theta_{in}}{mf_0} \end{pmatrix}. \tag{7}$$

From Fig. 2 we can see that in the paraxial approximation, *i.e.* $\sin(\theta) = \theta$,

$$R(\delta) = \frac{mf\theta_{in}}{-\frac{\delta\theta_{in}}{mf}} = -\frac{m^2 f^2}{\delta}. \tag{8}$$

Here $R(\delta)$ is the radius of curvature of the wave front at the phase plate. The optical path from the emitter to the wave front is equal for all rays. f, now dropping the index, is the focal length of the objective. In order to calculate the phase difference between the fields that pass through the inner and outer sections of the phase plate we first calculate the optical path delay as a function of the position y along the phase plate. We define the optical path delay $opd(y,\delta)$ as the difference between the optical path lengths to the phase plate for a ray intersecting the phase plate at y and for the chief ray for which y = 0:

#166541 - $15.00 USD Received 12 Apr 2012; revised 23 May 2012; accepted 25 May 2012; published 22 Jun 2012

$$opd\left(y,\delta\right)=\sqrt{R\left(\delta\right)^2+y^2}-R\left(\delta\right). \tag{9}$$

For large $R(\delta)$, i.e. for small δ,

$$opd\left(y,\delta\right)\approx\frac{1}{2}\frac{y^2}{R}=\frac{1}{2}\frac{y^2\delta}{m^2f^2}. \tag{10}$$

The average optical path delay over a section of the phase plate from $r = a$ to $r = b$, where r is the radius of a disk on the phase plate, is then given by the 2D integral

$$opd_{avg\,2D}\left(a,b,\delta\right)=\frac{\int_0^{2\pi}\int_a^b opd\left(r;\delta\right)e^{-\frac{r^2}{w^2}}rdrd\phi}{\int_0^{2\pi}\int_a^b e^{-\frac{r^2}{w^2}}rdrd\phi}, \tag{11}$$

where w is the width of the Gaussian profile of the scaled fiber mode field at the phase plate. This weighting of the average with the Gaussian mode field is necessary because the single mode fiber will accept only the embedded Gaussian beam that matches the fiber mode field. The phase difference (in radians) of the interference spectra obtained with source locations $\delta = 0$ and $\delta = z$ for a set-up with a phase plate of radius ρ is now given by:

$$\Delta\phi=\frac{2\pi}{\lambda}\left(opd_{avg\,2D}\left(\rho,\infty,\delta\right)-opd_{avg\,2D}\left(0,\rho,\delta\right)\right) \tag{12}$$

where λ is the wavelength of the light. Using Eq. (12) and substituting $z_R=\lambda f^2/\pi w^2$ for the Rayleigh length z_R we find $\Delta\phi/z_R=1.33\,\mathrm{rad}/z_R$. Under these conditions, phase wrapping occurs only at ± 2.4 Z_R, where the confocal system rejects virtually all light; therefore, phase wrapping does not cause depth ambiguity.

3. Self-interference fluorescence microscope

To demonstrate the capabilities of this new imaging technique, a commercial microscope platform (Olympus IX71) was equipped with a home-built galvanometric x/y-scanner. A fiber coupled 635 nm Fabry-Perot diode laser (Thorlabs, S1FC635) was used as an excitation source (Fig. 3). All measurements reported were accomplished with a power of 650 µW at the sample. A dichroic mirror based wavelength division multiplexer (OZ Optics) was used to separate excitation and emission light. A home-built spectrometer based on a holographic transmission grating (1200 lpmm, Wasatch Photonics) and a CMOS line scan camera (spL4096-140km, Basler) was used to detect the fluorescence spectra. All measurements were performed at a line rate of 1 kHz (1000 spectra/s).

The limited sensitivity of the spectrometer camera used currently restricts the imaging speed because sufficient photons need to be collected for the signal to dominate the read noise of the camera. One way to improve this is to use a phase plate with a much smaller optical path difference. With an optical path difference that results in only one modulation period over the spectral bandwidth of the fluorophore the phase of the modulation can be detected with only three detector elements. If one uses highly sensitive photomultiplier tubes or avalanche photodiodes the sensitivity, and therefore the imaging speed, of SIFM is comparable to standard confocal microscopy.

The phase plate consisted of a standard 1 mm microscope slide with a 4 mm diameter hole. This was placed into the collimated beam in front of the x/y-scanner in the virtual back focal plane of the objective. The Gaussian beam waist (radius of $1/e^2$ intensity drop-off) at the phase plate was 2.59 mm. This value was calculated based on the fiber numerical aperture

#166541 - $15.00 USD Received 12 Apr 2012; revised 23 May 2012; accepted 25 May 2012; published 22 Jun 2012

reported by the manufacturer and the focal length of the collimator. The 4 mm diameter hole for the phase plate was close to the optimal value of 4.14 mm for the 2.59 mm Gaussian beam waist. The optical path delay introduced by the 1 mm phase plate with a refractive index of 1.5 was 500 µm. This led to a modulation period of $2\pi / 5 \cdot 10^{-4} = 12560\ m^{-1}$ according to Eq. (1). At the center wavelength of the fluorescence (755 nm) this corresponded to a period of 1.1 nm^{-1} which was easily resolved by the current spectrometer. An interpolation of the spectra was performed to linearize the data in k-space before the Fourier transformation.

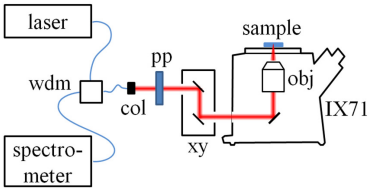

Fig. 3. Schematic representation of the SIFM microscope. Excitation light from a fiber coupled laser is sent through a wavelength division multiplexer (wdm) and a collimator (col) before passing through a phase plate (PP). The beam is sent into the microscope (IX71) via a home-built galvanometric x/y-scanner (xy) and is focused onto the sample by the objective (obj). The fluorescence is collected by the same objective and follows the same light path in the opposite direction to the wdm where it is sent to a home-built spectrometer that detects the interference spectra.

4. Results and discussion

4.1 Depth sensitivity

Figure 4(a) shows the axial position dependence of the phase of the self-interference spectrum. A thin layer of fluorescent polymer beads was prepared by filling a 50 µl µ-Slide (Ibidi) with fluorescent polymer beads (fluospheres 715/755, Invitrogen, 100 nm, 0.2% by weight) and drying slowly to the air. This thin homogeneous fluorescent layer was moved through the focus of the SIFM microscope. We used a 4x objective (UPLSAPO 4X, Olympus) with a nominal NA of 0.16. The objective was underfilled by a Gaussian beam with a waist of 1.94 mm leading to an effective NA of 0.086. For each datapoint, 1024 fluorescence spectra were recorded at the same lateral position with an integration time of 1 ms per spectrum.

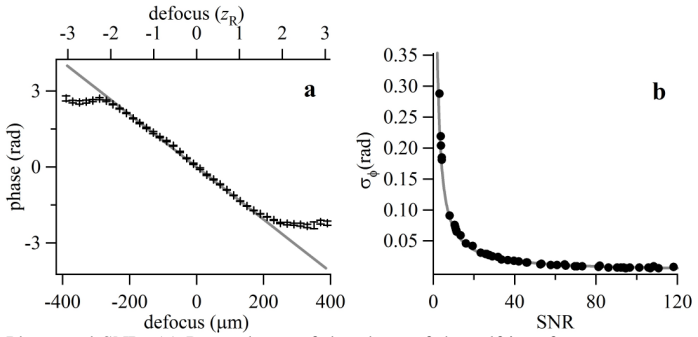

Fig. 4. Phase and SNR. (a) Dependence of the phase of the self-interference spectrum on the axial position of a thin homogenous fluorescent layer with respect to the focal plane of the objective. Each datapoint is the mean value from 1024 spectra. The error bars indicate ± 1 standard deviation. The imaging NA for this measurement was 0.086 (using the approximate definition for the NA of Gaussian beams: $NA \approx 2\lambda / \pi w_0$) and the Rayleigh length $z_R$was 128 µm. A linear fit of the central section between −2 and $2z_R$ yields a slope $d\phi/dz = -1.31$ rad/z_R. A simple ray optics analysis of the system predicts a slope of −1.33 rad/z_R indicated by the solid gray line. (b) Dependence of the standard deviation of a phase measurement on the signal to noise ratio. Here the SNR was varied by scanning the fluorescent layer through the focus of the objective. The dots are the measured standard deviations of 1024 phase measurements. The solid line is the theoretical curve $\sigma_\phi = 2^{-1/2} \cdot SNR^{-1}$.

#166541 - $15.00 USD Received 12 Apr 2012; revised 23 May 2012; accepted 25 May 2012; published 22 Jun 2012

From these spectra, the mean and standard deviation were calculated of the total intensity and the phase of the fringes. The central section of Fig. 4(a), from −250 to 250 μm, clearly shows a linear dependence of the phase on the depth position z, with a slope of $d\phi / dz = -10.2$ rad/mm. Using the ray transfer matrix model described above the dependence of the phase on the axial position of the source was calculated. The predicted slope was $1.33\,\text{rad}/z_R$ with z_R the Rayleigh length (128 μm) of the optical system, based on the numerical aperture ($NA = 0.086$), the phase plate geometry, and the mode field diameter as reported by the fiber manufacturer. The solid gray line in Fig. 4(a) indicates the slope of the phase predicted by our theoretical model of the optical system, which is in excellent agreement with the measured data. The smallest and largest standard deviation measured in the linear regime is 6.7 and 39 mrad, with corresponding SNRs of 114 and 30, respectively. These standard deviations were within 1.1 to 1.7 times the theoretically predicted standard deviations based on the SNR. The smallest and largest standard deviations using this SIFM system correspond to a depth sensitivity of 0.7 to 4 μm, respectively, compared to the large (500 μm) depth of field. Here, we define the depth of field as four times the Rayleigh length, which is determined by the numerical aperture. The depth-of-field scales with $1/NA^2$ while the lateral resolution scales with $1/NA$, similar to standard confocal microscopy. In order to achieve a large depth-of-field one needs to use a low NA and therefore sacrifice some lateral resolution.

As the depth position accuracy is defined by the system SNR and objective NA, far higher localization accuracy can be obtained by either simply collecting more photons or by choosing a higher NA objective. Figure 4(b) shows the excellent agreement between measured σ_ϕ as a function of the SNR and theory. The solid gray line is the theoretical curve $\sigma_\phi = 2^{-1/2} \cdot SNR^{-1}$. In the shot noise limit, with only 100 collected photons per spectrum (SNR = 5), the phase noise σ_ϕ is predicted to be 0.14. This translates to a depth position standard deviation of 13 μm when using a low NA of 0.09. If one instead uses a high 1.2 NA water immersion objective, this depth position error shrinks to an accuracy of just 73 nm. It is worth noting that these resolutions can be achieved even when imaging in the near infrared.

4.2 Three dimensional imaging

To illustrate the 3D imaging capabilities of SIFM and to validate the depth information collected in a single 2D SIFM scan, a thick sample was imaged using both SIFM and standard confocal microscopy.

400 mg agarose was dissolved in 20 ml filtered water (milli-Q) by boiling. This hot solution was quickly mixed with 50 μl bead solution (1 μm fluospheres 715/755, Invitrogen). The warm solution was quickly pipetted into a 150 μm high microfluidic channel made with a microscope slide, a coverslip and double sided tape. The channel was sealed with a 1:1:1 mixture of vaseline, lanoline and paraffin.

For SIFM, the focus was placed 75 μm into the gel using a 20x objective (Olympus UPlanSApo 20X, underfilled to an effective NA of 0.43) and scanned over a single 125 × 125 μm lateral plane. The resulting intensity image, Fig. 5(a), clearly shows the beads distributed in the gel matrix. In the corresponding phase image, Fig. 5(b), each pixel is colored according to its own unique phase. From these phase values, the depth of each emission source was assigned to a corresponding voxel in a 125 × 125 × 30 μm 3D volume.

#166541 - $15.00 USD Received 12 Apr 2012; revised 23 May 2012; accepted 25 May 2012; published 22 Jun 2012

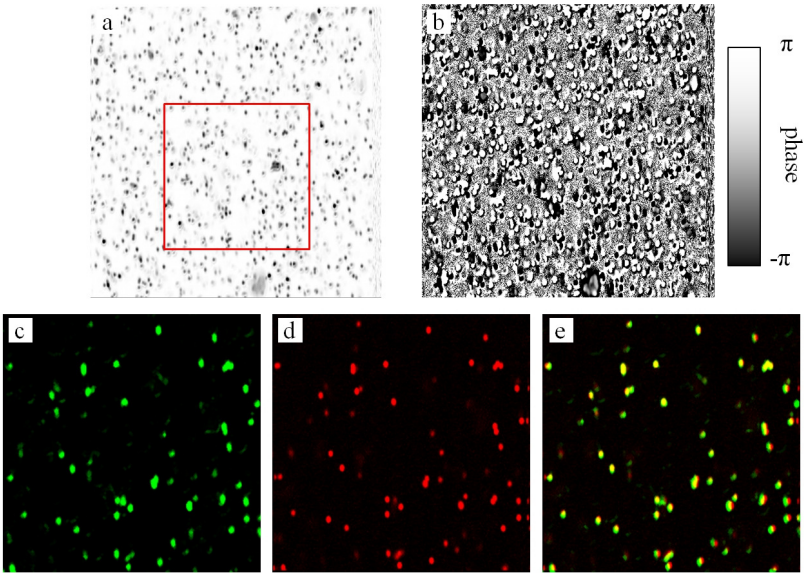

Fig. 5. Comparison of SIFM and confocal microscopy on a three-dimensional distribution of fluorescent microspheres. (a) SIFM intensity image (100 × 100 µm). The red square marks the area that was compared to a standard confocal stack. (b) SIFM phase image. (c) Representative slice from the SIFM 3D reconstruction. (d) Corresponding slice from the confocal stack. (e) SIFM and confocal slices overlapped. SIFM data displayed in green and confocal in red. Yellow indicates the overlap of both data sets. A video that shows the overlap of the data sets for the whole volume is available online (Media1).

After the SIFM volume was collected, the 20x objective was replaced by a high-NA 60x objective (Olympus, UPlanSApo 60XW) mounted on a piezoelectric z-scanner (PI, P-725.2CD). The phase plate was then removed from the setup so as to collect a standard confocal image stack. Thirty images were collected over a lateral area of 65 × 65 µm (red square in Fig. 5(a)) with a depth spacing of 1 µm each. Figures 5(c) and 5(d) show a representative slice through the reconstructed 3D SIFM volume and the corresponding slice from the confocal stack, respectively. The axial point spread function using the 60x objective was found to be 2.1 µm (FWHM) for 755 nm emission. In order to facilitate the comparison of the SIFM and confocal data, the SIFM stack was convolved with a Gaussian with a width (FWHM) of 2 µm in the z direction. An erode/dilate filter with a radius of 190 nm was subsequently applied. Figure 5(e) shows a composite image of the same optical slice acquired using SIFM (green) and confocal microscopy (red). The co-localization of beads in the combined images is excellent, demonstrating that SIFM volumes of comparable quality to confocal imaging can be collected in just a single 2D scan over a much wider area in a much shorter period of time.

4.3 Mouse heart vasculature

In tissue, fluorescent emission can undergo multiple scattering events while propagating to the objective due to the turbid microenvironment. One could expect that multiple scattering events distort the spherical wave fronts emitted by the fluorophore, posing a significant challenge to this technique or affecting the self-interference pattern. To demonstrate that SIFM works even in the presence of tissue scattering, the vasculature of an *ex vivo* mouse heart was imaged.

A C57BL/6 mouse was anesthetized and subsequently sacrificed with avertin according to standard procedure. A cut was then made in the right ventricle and saline perfusion solution was injected into the left ventricle until all blood was removed from the circulation. The mouse was then perfused with 0.5 ml of fluospheres (2% solids). The heart was removed and

#166541 - $15.00 USD Received 12 Apr 2012; revised 23 May 2012; accepted 25 May 2012; published 22 Jun 2012

imaged fresh using a 10x objective (Olympus UPlanSApo 10X, underfilled to an effective NA of 0.22). Animal housing, breeding and experiments were carried out in accordance to Dutch law and the Animal User Care Committee of the VU University.

Figure 6 shows a color-coded, three-dimensional map of the myocardial microvasculature obtained with a single 512 × 512 pixel raster scan without depth scanning. The highly oriented capillaries follow a pattern that is tightly associated with individual myocites (not visible in this image) [12, 13]. The SIFM volume also shows larger vessels connecting to the capillary bed.

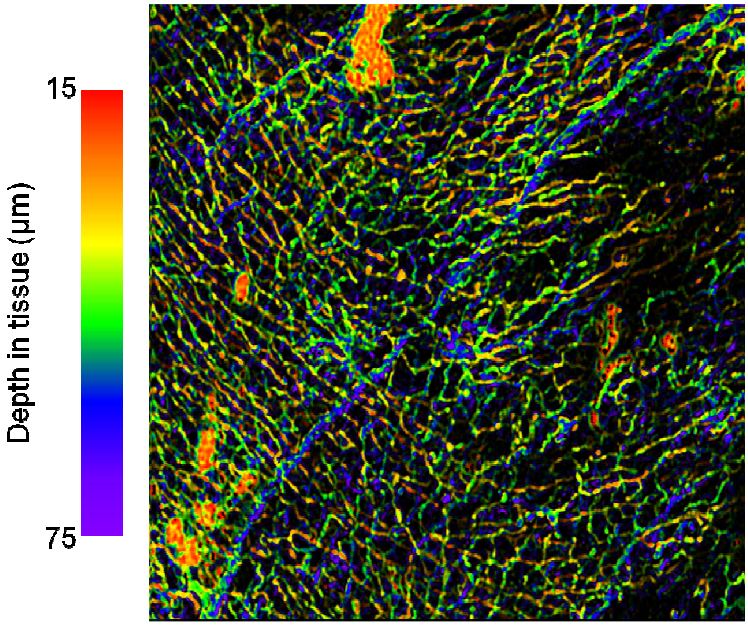

Fig. 6. SIFM image of microvasculature in a mouse heart. The image represents a 500 x 500 x 60 µm volume of tissue, starting at 15 µm below the tissue surface. (A) The depth of the vessels is color-coded: the deepest layers are displayed in violet and the top layers are displayed in red. (B) A movie that shows a three-dimensional rendering of the data is available online (Media 2).

5. Conclusions

In summary, we have introduced self interference fluorescent microscopy, a novel interferometric method to detect the depth position of a (fluorescent) emitter without depth scanning. By introducing a phase plate into the optical path of a standard confocal imaging system, we present the fluorescence photons with two alternative optical paths, thereby forcing them to self-interfere. The phase information of the spectrally resolved self-interference can be exploited to precisely measure the depth location of a fluorescent signal without any need for depth scanning. Self interference fluorescent microscopy can easily be integrated in any confocal imaging system and is especially suited for applications such as miniature endoscopy where space constraints pose a challenge to obtain depth information.

Acknowledgments

We would like to thank Joke Wortel and Ruud Toonen from the Center for Neurogenomics and Cognitive Research, Neuroscience Campus Amsterdam for their help with the animal experiments. This work was supported by the National Institutes of Health (project R21 RR023139). This work is part of the research program Vernieuwingsimpuls which is (partly) financed by the Netherlands Organization for Scientific Research (NWO).

#166541 - $15.00 USD Received 12 Apr 2012; revised 23 May 2012; accepted 25 May 2012; published 22 Jun 2012